

## Two-dimensional simulation of superlubricity on NaCl and highly oriented pyrolytic graphite

Pascal Steiner,<sup>\*</sup> Raphael Roth, Enrico Gnecco, Alexis Baratoff, Sabine Maier,<sup>†</sup> Thilo Glatzel, and Ernst Meyer  
*Department of Physics, University of Basel, Klingelbergstr. 82, 4056 Basel, Switzerland*

(Received 18 September 2008; revised manuscript received 21 November 2008; published 16 January 2009)

The friction between an atomically sharp tip and a solid surface (NaCl and highly oriented pyrolytic graphite) is analyzed theoretically in the framework of a modified Tomlinson model in two dimensions. Lateral forces are studied as a function of temperature, load, and magnitude of actuation. The actuation leads to a reduction in friction and allows one to enter a dynamic superlubricity regime. In addition, our model is able to describe other ultralow friction states as static superlubricity and thermolubricity. We find a good agreement between the calculations and the experimental results.

DOI: [10.1103/PhysRevB.79.045414](https://doi.org/10.1103/PhysRevB.79.045414)

PACS number(s): 68.35.Af, 07.79.Sp, 62.25.-g, 81.05.Uw

### I. INTRODUCTION

Macroscopic friction between solids is well known to be both of high practical importance and of notorious difficulty regarding its theoretical understanding. Technical solutions, such as bearings or liquid lubricants, can reduce friction at macroscopic dimensions, but in the microscopic range, for instance, in microelectromechanical or nanoelectromechanical systems (MEMS/NEMS) other approaches and ideas are required. The study of friction reduction in a single contact has gained relevance in the field of nanotechnology. Friction at the atomic range is ideally explored by friction force microscopy (FFM), in which a tip apex consisting of only a few atoms is dragged across a solid surface.<sup>1-5</sup> Theoretically, atomic scale friction in the absence of wear, plastic deformation, and impurities can be interpreted using simple ball-and-spring models as the Tomlinson model.<sup>6</sup> An overview of the field of computer simulations and theoretical modeling of friction, lubrication, and wear was recently given by Szlufarska *et al.*<sup>7</sup> There are several ways to reduce friction. First, when the normal load acting on the tip decreases below a critical threshold, the characteristic stick-slip motion is suppressed and sliding occurs smoothly without abrupt jumps and dissipation while the contact is maintained. This transition was observed by our group on ionic crystals in ultrahigh vacuum (UHV).<sup>8</sup> Second, ultralow friction is achieved while dragging two crystal surfaces out of registry against each other,<sup>9-11</sup> which is not discussed in this paper. Third, an actuation of the system at well-defined frequencies facilitates the reduction in friction as well. For instance, an excitation of the cantilever in normal direction at the contact resonance frequency leads again to a remarkable reduction in friction and dissipation, as shown by our group on ionic crystals, mica, and highly oriented pyrolytic graphite (HOPG).<sup>12,13</sup> The concept of ultralow friction is often referred to superlubricity.<sup>14</sup> Unfortunately, the first technique to achieve “static” superlubricity cannot be easily applied in practical situations because it requires detecting and maintaining constantly very small loads, and in addition, a switching between the usual state and the superlubricity state is not feasible. Hence the latter technique is more promising because higher loads are allowed and a switching between the usual dissipative state and the “dynamic” superlubricity state is possible. In this paper, we report an extension of the theoret-

ical model, which describes the different types of superlubricity for different substrates in two dimensions including thermal effects.

### II. MODEL

The system is described in terms of a simple model which is essentially a two-dimensional Tomlinson model<sup>6</sup> for one asperity. The surface is modeled as a rigid lattice with square periodicity in the case of NaCl and trigonal periodicity in the case of HOPG. The tip is handled as a point mass that is coupled to a support (“chip of the cantilever”) by springs in the  $x$  and  $y$  directions. Via these springs, the tip is dragged over the periodic lattice. The interaction of the tip with the atomic surface of NaCl is described by an adiabatic potential  $V_{\text{NaCl}}(\vec{r}_{\text{tip}})$ ,<sup>15</sup> which corresponds to the first term of the two-dimensional Fourier series and has the form

$$V_{\text{NaCl}}(x,y) = -\frac{E_0}{2} \cos\left(\frac{2\pi}{a}x\right) \cos\left(\frac{2\pi}{a}y\right), \quad (1)$$

where  $a=0.564$  nm and  $(x,y)$  is the tip position. In the case of HOPG the interaction potential between tip and surface is described very similar to the potential used by Verhoeven *et al.*<sup>10</sup>

$$V_{\text{HOPG}}(x,y) = -\frac{E_0}{4.5} \left[ 2 \cos\left(\frac{2\pi}{a}x\right) \cos\left(\frac{2\pi}{a\sqrt{3}}y\right) + \cos\left(\frac{4\pi}{a\sqrt{3}}y\right) \right], \quad (2)$$

with  $a=0.246$  nm as determined by the unit-cell parameters of the HOPG surface. Furthermore, both lattices can be rotated by a simple coordinate transformation, whereas the [100] direction is defined as  $0^\circ$  in both NaCl and HOPG (see Fig. 1). It has to be mentioned that in the case of NaCl, only one sort of atom is observed in the experiment, depending on the ionic kind of the furthestmost atom of the tip apex.<sup>16</sup> In the case of HOPG, only the “hollow” sites of the hexagonal carbon rings are imaged (which represent the potential minima) and not the profile of the maxima of the interaction potential (i.e., the positions of the carbon atoms). This leads to a threefold symmetry with a distance of 0.246 nm between the minima.<sup>17</sup> Both  $V_{\text{NaCl}}(\vec{r}_{\text{tip}})$  and  $V_{\text{HOPG}}(\vec{r}_{\text{tip}})$  represent the

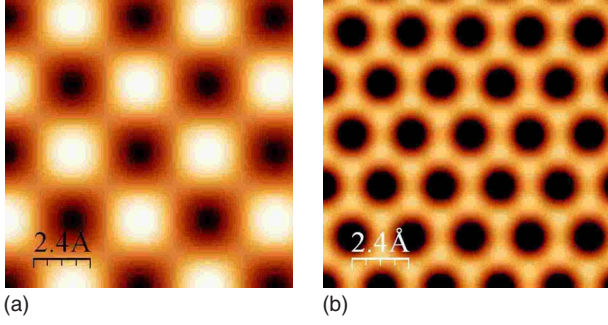


FIG. 1. (Color online) Potential-energy surface of (a) NaCl and (b) HOPG with a side length of 1.2 nm. The unit-cell parameter is 0.564 nm for NaCl and  $0.246 \times 0.426$  nm<sup>2</sup> for HOPG. In NaCl only one sort of atom is visible, depending on the tip apex. HOPG has a trigonal lattice because only the potential minima are detected (in the experiment).

shape of the periodic lattice and have to be multiplied by a constant in order to obtain the corrugation potential amplitude  $E_0$ . The amplitude  $E_0$  is related to the tip-sample interaction (and thus to the externally applied load) in the experiment and is assumed to obey a linear dependence with respect to the load. This assumption is valid only for the repulsive regime and as long as no deformation occurs, which is usually the case for experiments in the low-nanonewton range. The total potential energy including the elastic energy stored in the springs is given by

$$V(\vec{r}_{\text{tip}}, \vec{r}_{\text{sup}}) = V_{\text{NaCl, HOPG}}(\vec{r}_{\text{tip}}) + \frac{1}{2}k(|\vec{r}_{\text{tip}} - \vec{r}_{\text{sup}}|)^2, \quad (3)$$

where  $\vec{r}_{\text{tip}} = (x, y)$  is the position of the tip and  $\vec{r}_{\text{sup}} = (x_{\text{sup}}, y_{\text{sup}})$  is the position of the (microscope) support, and  $k = k_{x\text{-eff}} = k_{y\text{-eff}} = 2$  N/m is the elastic spring constant in the  $x$  and  $y$  directions (see the Appendix), whereas the scanning direction is defined as the  $x$  axis. The lateral force acting on the support is simply given by Hooke's law

$$F_L = -k(x_{\text{sup}} - x). \quad (4)$$

In FFM experiments, the lateral force  $F_L$  is measured only in the scanning direction. Therefore only the force acting on the support in the  $x$  direction is considered as the friction force. In Secs. II A and II B, two different methods are applied to determine the tip motion and the lateral force. In the first method, the equation of motion of the tip at finite temperatures is solved, assigning a finite mass to the tip and introducing a viscous force hindering the tip motion. In the second method, analytical expressions are determined in the so-called quasistatic limit, where the tip motion is quite slow. The results of the numerical simulations have been analyzed and converted into images by means of the WSXM software.<sup>18</sup>

### A. Langevin equation

The dynamics of the tip on the surface at finite temperatures can be described by the Langevin equation<sup>19–21</sup>

$$m \frac{d^2x}{dt^2} + m\gamma \frac{dx}{dt} + \frac{\partial V(\vec{r}_{\text{tip}}, \vec{r}_{\text{sup}})}{\partial x} = \xi(t). \quad (5)$$

The effective mass of the tip is assumed to be  $m = 10^{-12}$  kg. Since there is no experimental estimate for the effective mass of the tip that corresponds to the stiffness of the tip,  $m$  was varied by several orders of magnitude for the simulation but was found to have no significant influence on the key results presented in this paper. Because the mass of the cantilever is many orders of magnitude larger than the mass of the tip, the thermal effects on the cantilever may be neglected. The Langevin equation for the  $y$  direction is defined in the same manner. In addition to the Newton equation of motion, a term  $\xi(t)$  is added which represents the Brownian motion of the tip.  $\xi(t)$  is a Gaussian distributed random noise satisfying the fluctuation-dissipation theorem

$$\langle \xi(t)\xi(t') \rangle = 2m\gamma k_B T \delta(t - t'), \quad (6)$$

where the angular brackets denote the mean,  $k_B$  is the Boltzmann constant,  $\delta(t - t')$  is the delta function, and  $\gamma$  is the damping coefficient of the tip movement. The temperature in the simulation is controlled and set to room temperature via  $\xi(t)$ . The Langevin equation is solved with an integration algorithm. A commonly used integrator for “Brownian dynamics” simulations is used, which is referred to the Ermak algorithm.<sup>22</sup> This algorithm is an attempt to treat properly both the stochastic and dynamic elements of the Langevin equation. At low values of the damping coefficient  $\gamma$ , the dynamical aspects dominate, and the Newtonian mechanics recover as  $\gamma \rightarrow 0$ . The damping coefficient  $\gamma$  is set to ten times the critical damping  $\gamma_{\text{critical}} = 2\sqrt{k/m}$ . An overdamped motion of the apex is typical for nanoscale systems and avoids oscillations of the tip. Hence the overdamped system is always in an adiabatic state, as is assumed in the quasistatic Tomlinson model.<sup>23</sup> Following the conditions of the experiment, the simulation is performed at room temperature and for a constant scan velocity of  $v = 25$  nm/s. An appropriate time step of  $\Delta t = 10^{-7}$  s is used for the support movement to achieve reasonable computation time without introducing artifacts.

### B. Quasistatic limit

At low temperature, the equation of motion of the tip can be solved analytically in a quasistatic limit, corresponding to very low tip velocities, and is only suitable at very low temperatures. In such a case, the tip resides most of the time in the minima of the potential-energy landscape  $V(\vec{r}_{\text{tip}}, \vec{r}_{\text{sup}})$  [see Eq. (3)] and “jumps” from one minimum into an adjacent minimum when the driving force exerted by the support overcomes a critical threshold.<sup>24</sup> In the minimum positions the condition  $\nabla V(\vec{r}_{\text{tip}}, \vec{r}_{\text{sup}}) = 0$  has to be satisfied. Substituting  $\vec{r}_{\text{sup}} = (vt, y_{\text{sup}})$ , where  $v$  is the velocity of the support and  $y_{\text{sup}}$  is a constant, one can easily see that the tip trajectory is defined by the condition  $\partial V / \partial y = 0$ , whereas  $\partial V / \partial x = 0$  gives the time dependence of the tip coordinates. Using Eq. (3) in the condition  $\partial V / \partial y = 0$ , we get

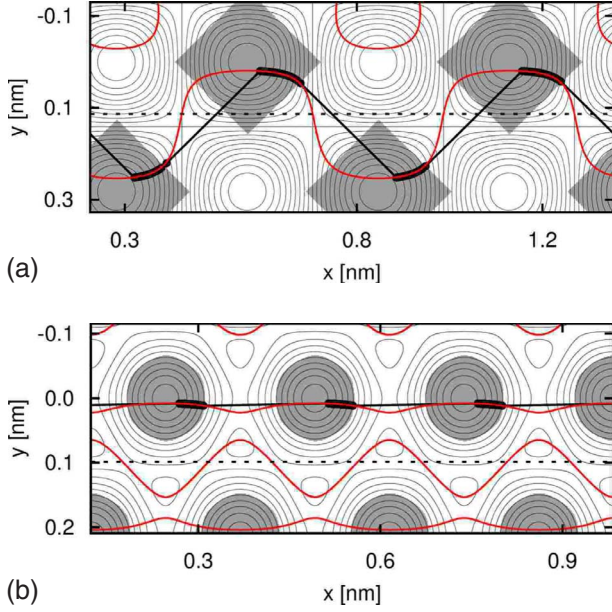


FIG. 2. (Color online) Contour plot of the potential  $V_{\text{NaCl,HOPG}}(x,y)$  for (a) NaCl with  $E_0=1$  eV and (b) HOPG with  $E_0=0.5$  eV. The horizontal dashed line indicates the scanning line with (a)  $y_{\text{sup}}=0.2a$  and (b)  $0.4a$ . Gray regions correspond to  $\lambda_{1,2} > 0$ . A superposition of the gray regions with the tip trajectory (red), where  $\partial V / \partial y = 0$ , leads to the analytical stick-slip motion of the tip and is in very good agreement with the numerical solution at 0 K (black points connected by lines).

$$\frac{E_0\pi}{a} \cos\left(\frac{2\pi}{a}x\right) \sin\left(\frac{2\pi}{a}y\right) + k(y - y_{\text{sup}}) = 0 \quad (7)$$

for the tip trajectory on NaCl and

$$\frac{8E_0\pi}{9\sqrt{3}a} \left[ \cos\left(\frac{2\pi}{a}x\right) \sin\left(\frac{2\pi}{a\sqrt{3}}y\right) + \sin\left(\frac{4\pi}{a\sqrt{3}}y\right) \right] + k(y - y_{\text{sup}}) = 0 \quad (8)$$

on HOPG. Examples for these tip trajectories on NaCl and HOPG are shown in Fig. 2. However the tip can only reside at points where the system is in stable equilibrium. In order to define these positions, the Hessian matrix  $\mathcal{H} = (\partial^2 V / \partial x_i \partial x_j)$  of the total potential is evaluated and its two eigenvalues  $\lambda_{1,2}$  are determined.<sup>15,25</sup> These eigenvalues have the form

$$\lambda_{1,2}^{\text{NaCl}} = k + \frac{2E_0\pi^2}{a^2} \cos\left(\frac{2\pi}{a}x \pm \frac{2\pi}{a}y\right) \quad (9)$$

in the case of NaCl and

$$\begin{aligned} \lambda_{1,2}^{\text{HOPG}} = k + \frac{16E_0\pi^2}{27a^2} & \left\{ 2 \cos\left(\frac{2\pi}{a}x\right) \cos\left(\frac{2\pi}{a\sqrt{3}}y\right) \right. \\ & + \cos\left(\frac{4\pi}{a\sqrt{3}}y\right) \pm \left[ \cos^2\left(\frac{2\pi}{a}x\right) \cos^2\left(\frac{2\pi}{a\sqrt{3}}y\right) \right. \\ & \left. \left. + \cos^2\left(\frac{4\pi}{a\sqrt{3}}y\right) + 3 \sin^2\left(\frac{2\pi}{a}x\right) \sin^2\left(\frac{2\pi}{a\sqrt{3}}y\right) \right] \right\} \end{aligned}$$

$$- 2 \cos\left(\frac{2\pi}{a}x\right) \cos\left(\frac{2\pi}{a\sqrt{3}}y\right) \cos\left(\frac{4\pi}{a\sqrt{3}}y\right) \Bigg]^{1/2} \quad (10)$$

for HOPG. The equilibrium is stable in the regions defined by the conditions  $\lambda_{1,2} > 0$ . The stability regions corresponding to potentials (1) and (2) are shown in Fig. 2 as well. When either  $\lambda_1 < 0$  or  $\lambda_2 < 0$ , the stability is lost and the tip suddenly jumps.

The analytical description of the tip movement has been compared to numerical solutions of Eq. (5) at 0 K. In the stability regions, a very good agreement between analytical and numerical results is observed (see Fig. 2). When the borders of these regions are reached, the numerical results suggest that the tip follows a straight line until it reaches the next stable position defined by curves (7) or (8). We note that numerical simulations of the tip trajectory on graphite were already shown by Fusco and Fasolino;<sup>26</sup> however they were not compared to analytical expressions.

### III. RESULTS

#### A. Lateral spring constants

Lateral force maps computed for three different ratios of the  $x$ - and  $y$ -spring constants are shown in Fig. 3. The obtained stick-slip patterns all show the expected lattice periodicity but are qualitatively different. As illustrated in Fig. 3(a), if the spring constant in the  $y$  direction is lower than the spring constant in the  $x$  direction ( $k_{x\text{-eff}} > k_{y\text{-eff}}$ ), stripes appear perpendicular to the scan direction, which are not observed in the experiments.<sup>13</sup> If the spring constant in the  $y$  direction is significantly higher than the spring constant in the  $x$  direction ( $k_{x\text{-eff}} \ll k_{y\text{-eff}}$ ), the friction pattern in each unit cell [see Fig. 3(c)] is distinctly different from that observed in the experiment. Only if the spring constants are chosen in the same range [ $k_{x\text{-eff}} \approx k_{y\text{-eff}}$ , see Fig. 3(b)], the rhombus shaped patterns observed on NaCl (Ref. 13) as well as on KBr (Refs. 27 and 28) are reproduced. A similar dependence on the ratio between the spring constants for the  $x$  and  $y$  directions is found in the case of HOPG, as demonstrated in earlier atomistic simulations.<sup>29</sup>

Our conclusion is that the effective spring constants  $k_{\text{eff}}$  for the  $x$  and the  $y$  directions are in the same range. As shown in the Appendix, the lateral spring constants  $k_{\text{lateral}}$  for both directions are also in the same range. This implies that the contact stiffness is isotropic ( $k_{x\text{-contact}} \approx k_{y\text{-contact}}$ ). This result might be expected for a symmetric tip, but it was not demonstrated before, last but not least, because the relevant parameters cannot be measured with a conventional FFM. Another important conclusion is that the lateral force patterns hitherto observed on cleaved alkali halides cannot be satisfactorily explained by a one-dimensional Tomlinson model.

#### B. Corrugation potential amplitude

The maximum absolute value of the lateral force is proportional to the amplitude  $E_0$  of the corrugation potential<sup>8</sup> and can therefore be experimentally determined from maps

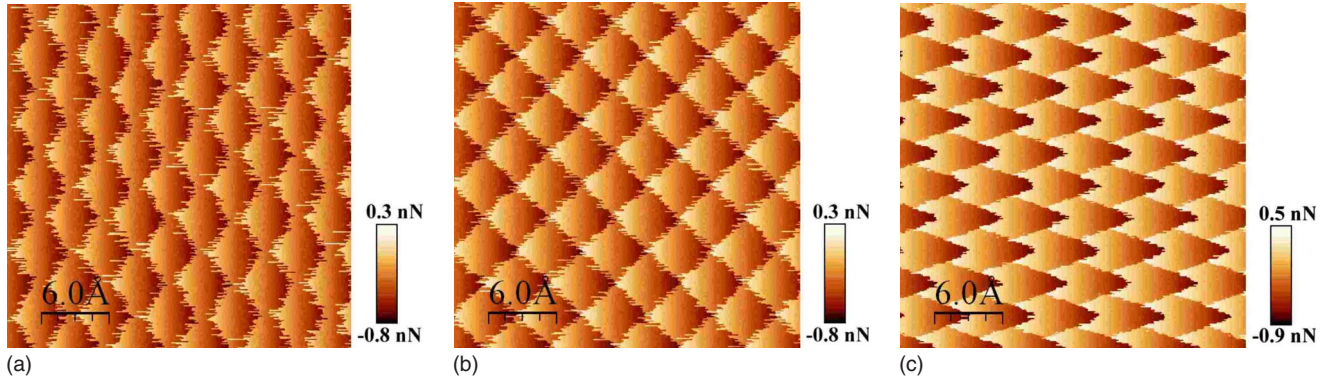


FIG. 3. (Color online) Calculated lateral force map of NaCl (forward scan direction) for different spring constants in the  $y$  direction, (a)  $k_{y\text{-eff}}=1$ , (b) 2, and (c) 10 N/m, whereas the spring constant in the  $x$  direction  $k_{x\text{-eff}}=2$  N/m is retained. The movement of the tip is heavily damped; thus an overshooting or jump over two lattice constants is avoided and the stick-slip behavior is sustained. The lateral force maps reveal different patterns; however a good agreement with experiment is only achieved when  $k_{x\text{-eff}} \approx k_{y\text{-eff}}$ . The amplitude of the corrugation potential is  $E_0=1$  eV.

similar to those shown in Fig. 3. The amplitude  $E_0$  depends on the mean tip-sample distance, which can in turn be controlled by the applied load in actual experiments. A linear dependence has been found between  $E_0$  and the mean normal force in experiments on NaCl (Ref. 8) and HOPG (Ref. 30) in a limited “soft contact” range, where no wear or plastic deformation occurs. The average friction force  $\bar{F}_L$  is calculated over a reduced scan area, so that the longer initial stick component of each scan line is removed because it does not contribute to the average friction force corresponding to periodic stick-slip events. A linear dependence of the average friction force  $\bar{F}_L$  on the amplitude  $E_0$  is only obtained at relatively high values of  $E_0$ , as shown in Fig. 4. When  $E_0$  falls below a critical threshold, the system enters into an ultralow friction regime, where the average friction force practically vanishes ( $\bar{F}_L \approx 0$ ). Both features, the linear dependence of the average friction force at high loads and the appearance of an ultralow friction state at loads below a critical threshold, were observed on NaCl in UHV by our group.<sup>8</sup> In the experiment, friction could not be detected in the ultralow friction regime because of an insufficient signal-to-noise ratio. In the simulation the average friction force  $\bar{F}_L$  is not equal to zero but is in the piconewton range. This value is consistent with the assumed parameters, i.e.,

$$\bar{F}_L = -m\gamma v = -0.7 \text{ pN}. \quad (11)$$

Finite damping always implies a net energy loss. However, the jump instabilities, which give the dominant contribution to the observed dissipation under stick-slip conditions, disappear in the superlubricity regime.

A comparison was performed to a one-dimensional simulation along a line with maximal corrugation. Figure 4 indicates that the absolute value of the average friction force  $\bar{F}_L$  is lowered in two dimensions because the tip avoids passing the maxima of the corrugation potential due to a zig-zag movement.<sup>15,29</sup> A noticeable consequence is that the one-dimensional Tomlinson model parameters, extracted from fits

to scan lines showing maximum lateral force variations, actually describe the potential profile along the corresponding zig-zag path rather than along the scan line *per se*.

### C. Temperature dependence

By increasing the temperature the probability for the tip to jump into an allowed adjacent minima is enhanced.<sup>3,31</sup> This leads to an earlier jump of the tip compared to lower temperatures, even though the energy barrier between the two minima remains finite. Above a critical temperature  $T_{\text{critical}}$  the thermally activated jumps thus reduce the average friction force. Below the critical temperature  $T_{\text{critical}}$ , the average friction force approaches  $\bar{F}_L = -m\gamma v$  and falls below the detection limit in the experiments. Due to the thermal effect

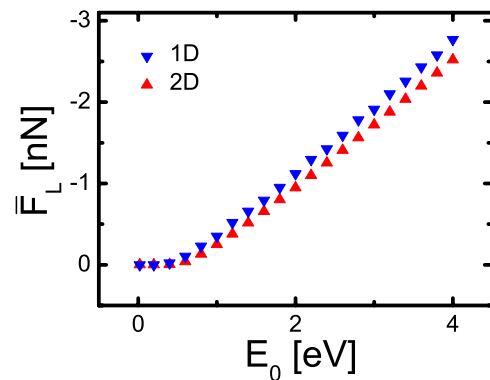


FIG. 4. (Color online) Average friction force  $\bar{F}_L$  for NaCl versus amplitude  $E_0$  of the corrugation potential. The amplitude  $E_0$  increases with the externally applied load in the experiment and shows a linear relation to the average friction force  $\bar{F}_L$ . However below a critical threshold of  $E_0$ , the linear relation goes over into an ultralow friction state where the average friction force  $\bar{F}_L \approx 0$ . In two dimensional the tip avoids passing the maximum of the corrugation potential, which leads to a zig-zag movement, and thus the average friction force  $\bar{F}_L$  is lowered compared to a one-dimensional simulation.

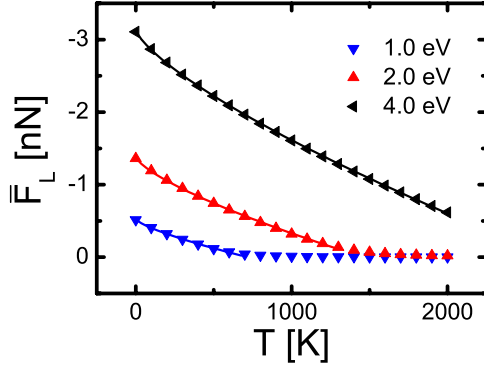


FIG. 5. (Color online) Temperature dependence of the average friction force  $\bar{F}_L$  for NaCl for different corrugation amplitudes  $E_0$ . Above a critical temperature  $T_{\text{critical}}$ , which depends on  $E_0$ , the system passes into the thermolubricity regime, where the average friction force  $\bar{F}_L \approx 0$ . The activation rate theory is in good agreement at lower temperatures (fitting curves) but cannot be applied to the thermolubricity regime, where the average friction force nearly vanishes.

that causes the reduction in friction, this kind of superlubricity has been called thermolubricity.<sup>32</sup> In Fig. 5 the computed average friction force  $\bar{F}_L$  is plotted for NaCl as a function of temperature for different  $E_0$ . The reduction in friction shows a nonlinear dependence on the temperature. According to the activation rate theory,<sup>20,31,33</sup> the absolute value of the average friction force  $\bar{F}_L$  deviates from its maximum value  $|\bar{F}_c|$  at  $T=0$ , with a correction of the form<sup>31</sup>

$$\bar{F}_c - \bar{F}_L \propto T^{2/3} \ln^{2/3} \left( \frac{cT}{v} \right), \quad (12)$$

where  $T$  is the temperature and  $c$  is a constant depending on other parameters. Below a critical temperature  $T_{\text{critical}}$ , which is proportional to the potential amplitude  $E_0$ , the analytical formula is in good agreement with our calculation (see fits of Fig. 5). We note that at ambient pressure NaCl has a melting temperature of 1074 K, which is far below the upper limit of 2000 K in the simulation. Atomic scale friction on NaCl close to the melting temperature was also explored by Zykova-Timan *et al.*<sup>34</sup> by molecular-dynamics simulations at high scan velocity of 50 m/s. Nevertheless, our model is not restricted to NaCl but is also applicable to other substrates which have much higher melting temperatures. For instance HOPG, which has a melting temperature of 3400 K, reveals the same dependence on the temperature. Even though the temperature only influences the tip movement in our model, the thermal activation of the substrate should also be considered. The velocity dependence<sup>31</sup> of the average friction force  $\bar{F}_L$  is not systematically investigated in this paper but is essential for the discussion of thermolubricity.<sup>32,35,36</sup> The following simulations are performed at room temperature in order to satisfy the conditions of most experiments.

#### D. Perpendicular actuation

An efficient way to “switch” friction on and off at the atomic scale is achieved by exciting mechanical resonances

of the sliding system perpendicular to the contact plane. This was demonstrated by our group on several surfaces as NaCl,<sup>12,13</sup> KBr,<sup>12</sup> mica,<sup>13</sup> and HOPG.<sup>13</sup> When the cantilever is excited in the normal direction, while the tip is still in contact with the surface, the distance between the tip and the sample slightly oscillates. The fundamental assumption is that the corrugation potential  $E_0$  oscillates with the frequency of actuation. Therefore the energy barrier between adjacent minima in the potential-energy landscape is also oscillating. The momentary lowering of the energy barrier allows the tip to move earlier to the adjacent minima compared to the case without actuation. Thus the atomic stick-slip curve can evolve into smooth sliding over the surface. As in the original simulation,<sup>12</sup> the corrugation amplitude  $E_0$  in Eqs. (1) and (2) is replaced by a time-dependent amplitude  $E(t)$ ,

$$E(t) = E_0[1 + \alpha \cos(2\pi ft + \phi)]. \quad (13)$$

We assume that the parameter  $\alpha$  is proportional to the strength of actuation amplitude in the experiment. Thus  $\alpha=0$  corresponds to the quasistatic case without actuation and  $\alpha=1$  to the maximum theoretically allowed actuation. The actuation frequency  $f$  corresponds to the flexural resonance frequency in contact in the experiment, but in the simulation an actuation frequency of  $f=2000$  Hz is used to keep reasonable computation times. The inertia and damping of the nanotip have a small effect in the adiabatic limit, where the forces acting on the tip are in balance at almost every instant. This leads to the following criteria:<sup>12</sup>  $f_{\text{tip}} \gg f$  and  $f\Gamma \ll 4\pi f_{\text{tip}}^2$ , where  $f_{\text{tip}} = \sqrt{k/m}/(2\pi)$  is the resonance frequency of the tip and  $\Gamma = \gamma/m$  is the damping rate of the tip. The additional criterion  $f \gg v/a$  ensures that the tip experiences the minimum corrugation many times within a lattice constant. A change in the actuation frequency  $f$  leads to a change in the number of minimum corrugations experienced by the tip within a lattice constant, but as long as the abovementioned conditions are fulfilled there is little influence on the main result. Furthermore, as long as the actuation frequency  $f$  is not a multiple of the so-called washboard frequency  $v/a$ , the phase shift  $\phi$  has no influence, which is the case in our simulation.

The effect of the time-dependent corrugation potential amplitude on the tip motion is illustrated for NaCl and HOPG in Fig. 6. In this case, the expressions for the tip trajectories [Eqs. (7) and (8)] and eigenvalues [Eqs. (9) and (10)] have to be modified by replacing  $E_0$  with  $E(t)$ . For visualization purposes, we consider only the extreme values  $E_0^+ = E_0(1 + \alpha)$  and  $E_0^- = E_0(1 - \alpha)$ . As in the one-dimensional case,<sup>8</sup> dynamic superlubricity is reached as soon as  $2E_0^- \pi^2 / ka^2 < 1$ . In this case, the stability regions cover periodically the entire potential-energy surface, allowing the tip to enter the stability region of adjacent minima. Hence, the nonadiabatic jumps of the tip are suppressed and thus also the energy dissipation. The oscillating potential-energy surface leads to a spatial oscillation of the tip path, which is enveloped by the curves  $\partial V(E_0^+) / \partial y = 0$  and  $\partial V(E_0^-) / \partial y = 0$ . If finite temperature effects are taken into account, these well-defined tip paths get delocalized by thermal fluctuations. For the sake of simplicity only the tip paths at  $T=0$  K are shown in Fig. 6.

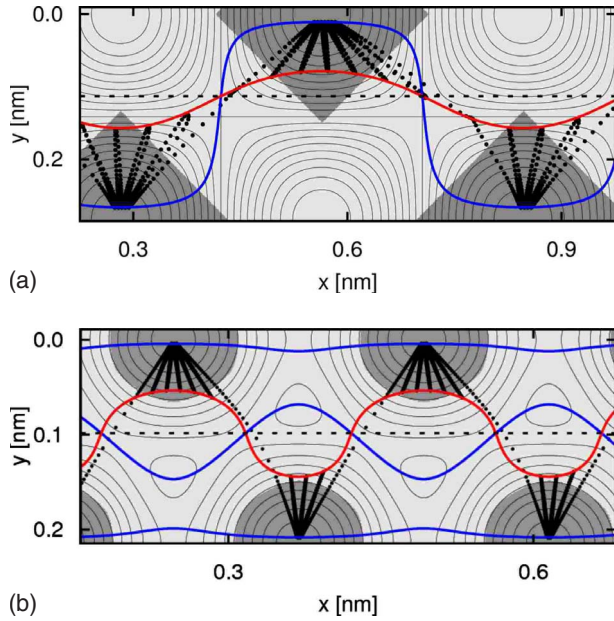


FIG. 6. (Color online) Tip paths at  $T=0$  K on (a) NaCl with  $E_0=1$  eV and (b) HOPG with  $E_0=0.5$  eV in the case of actuation with  $\alpha=0.9$ . The support paths with (a)  $y_{\text{sup}}=0.2a$  and (b)  $0.4a$  are indicated as dashed lines. The stability regions for  $E_0^+$  are mapped dark gray, while the corresponding stability regions for  $E_0^-$  cover the whole image (light gray). Analytic tip trajectories for the extreme cases  $E_0^+$  are plotted as blue lines and for  $E_0^-$  as red lines. Between these lines, the numerically calculated tip path (black dots) spatially oscillates and thus jumps are suppressed. For visualization reasons, the actuation frequency is lowered to  $f=500$  Hz.

Several simulations have been performed with different actuation amplitudes  $\alpha$  and corrugation amplitudes  $E_0$ . To reveal the differing features of the simulations with and without actuation, it is appropriate to switch on and off the actuation while generating an image. In Fig. 7 the results for NaCl and HOPG are presented.  $E_0=2$  eV for NaCl and  $E_0=1$  eV for HOPG are assumed, and actuation with  $\alpha=0.9$  is switched on in the lower half of the image. The number of pixels in both directions is set to 300, which is comparable to experiments, where typically  $256 \times 256$  pixels are recorded. An increase in the number of pixels has no influence on the main result, apart from increasing the computation time. The line scan in the forward direction (black) and backward direction (red) without actuation (upper half) exhibits the well-known stick-slip behavior that also causes a hysteresis loop [Figs. 7(c) and 7(e)]. The enclosed area of this hysteresis loop is equal to the energy that is lost during one scan cycle due to friction. Beyond the line where actuation is switched on, the profile changes dramatically. Instead of stick slip, the lateral force indicates continuous sliding on the surface. The forward and backward line scans are overlapping, and thus the hysteresis loop disappears [Figs. 7(d) and 7(f)]. This suppression of friction and of the associated energy dissipation is in agreement with the experiments and can be called dynamic superlubricity. Furthermore our results show that the more realistic two-dimensional Tomlinson model can account for the observed effects.

Next, the effect of varying actuation amplitude between  $\alpha=0$  and 1 is analyzed for several corrugation amplitudes  $E_0$ . The average friction force  $\bar{F}_L$  shows a linear dependence on the actuation strength (see Fig. 8) until  $\alpha$  approaches a critical value  $\alpha_{\text{critical}}$ , where the system enters into the superlubricity regime. This behavior resembles the temperature de-

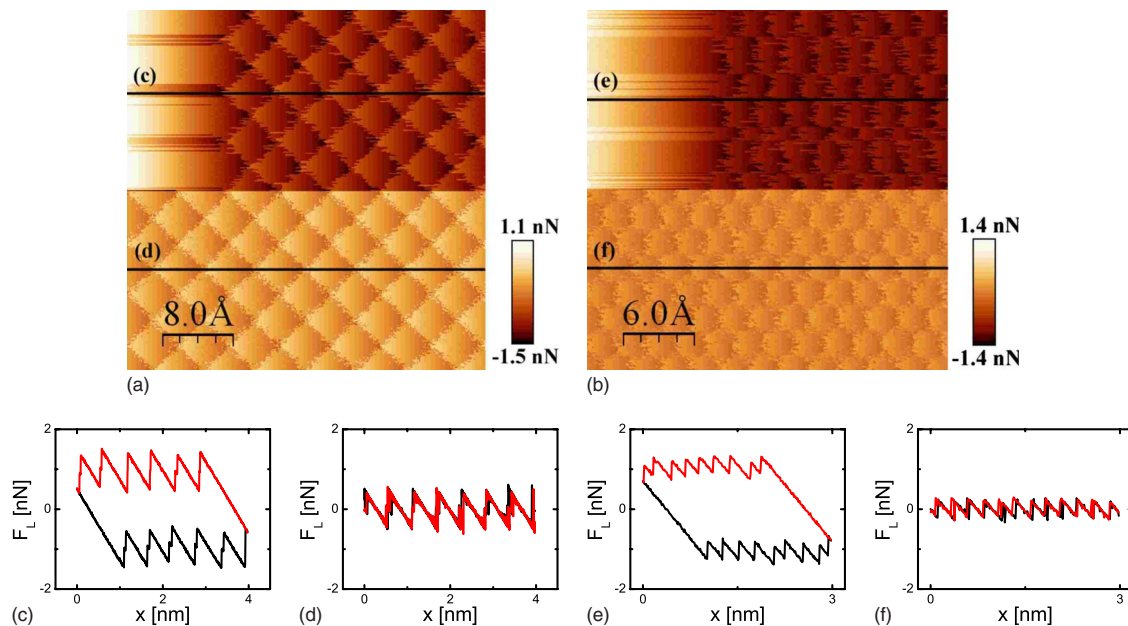


FIG. 7. (Color online) (a) Calculated lateral force map on NaCl using  $E_0=2$  eV (forward scan direction). In the upper part of the image is  $\alpha=0$ , whereas in the lower part actuation with  $\alpha=0.9$  is switched on. Typical line scans (black: forward; red: backward) on NaCl (c) without actuation showing a friction loop and (d) with actuation showing no hysteresis. (b), (e), and (f) are the analog lateral force map line scan profiles without and with actuation for HOPG using  $E_0=1$  eV.

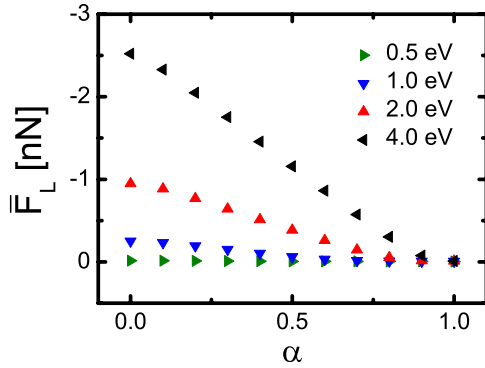


FIG. 8. (Color online) Average friction forces  $\bar{F}_L$  for three different corrugation amplitudes  $E_0$  on NaCl as a function of normalized actuation amplitude  $\alpha$ . For larger corrugation amplitude  $E_0$ , a stronger actuation is required to enter the superlubricity regime. For sufficiently small corrugation potential amplitude ( $E_0=0.5$  eV), the system is already in the superlubricity regime independent of actuation.

pendence, where the system enters into the thermolubricity regime above a critical temperature  $T_{\text{critical}}$ . The value of  $\alpha_{\text{critical}}$  strongly depends on the corrugation potential amplitude  $E_0$ . A smaller corrugation amplitude  $E_0$ , which can be adjusted by the load in the experiment, requires a weaker actuation to enter the superlubricity regime. In the extreme case of  $\alpha_{\text{critical}}=0$ , the system is already in the superlubricity regime even without actuation. In this case, the dynamic superlubricity state is superposed by the static superlubricity state because the corrugation amplitude  $E_0$  is below the critical threshold. In addition thermally activated jumps of the tip occur and reduce the average friction force at room temperature. This situation is presented in Fig. 8 for NaCl with a corrugation amplitude of  $E_0=0.5$  eV.

#### IV. CONCLUSION

Three different types of ultralow friction regimes are analyzed numerically with an extended two-dimensional Tomlinson model. First, the load dependence of friction reveals an ultralow friction regime when the normal load acting on the tip decreases below a critical threshold, as shown experimentally by Socoliuc *et al.*<sup>8</sup> The characteristic stick-slip motion is suppressed and sliding occurs smoothly and without abrupt jumps. This type of friction regime is often referred to as static superlubricity. Second, the temperature dependence predicts an ultralow friction regime when the temperature reaches a critical temperature. In that case, thermally activated jumps of the tip occur. The development of the sticking part is prevented by an early jump to the adjacent minima. This type of friction reduction is called thermolubricity<sup>32</sup> but was not shown experimentally up to now. Third, an externally applied actuation of the system facilitates the reduction in friction. For instance, an actuation of the cantilever in normal direction at the contact resonance frequency leads to an ultralow friction regime, as shown by Socoliuc *et al.*<sup>12,13</sup> Because an externally applied actuation is required, this type of ultralow friction regime is referred to dynamic superlu-

bricity. In all three cases, the simulation reveals that the average friction forces are not equal to zero in the ultralow friction regime, but they are found to be in the piconewton range. Hence they are below the experimental detection limit of the FFM.

Our present calculations are capable of describing the ultralow friction regimes originated from different mechanisms of friction reduction and are in good agreement with the experiments. The recently introduced mechanism of dynamic superlubricity has been discussed in details. We have shown how the tip trajectories, which are analytically and numerically estimated in the model cases of NaCl and HOPG, are modified by the external actuation. Here the tip oscillations smooth the jumps between adjacent minima, “opening the gate” to the superlubricity regime. Compared to the one-dimensional models presented so far, all three effects of friction reduction appear slightly enhanced in two dimensions. This result is important since it allows extending the one-dimensional formalism with only minor modifications. Future theoretical and experimental investigations should clarify how this picture is modified when larger and multiple contact areas, formed by more realistic adjoining surfaces, are taken into consideration.

#### ACKNOWLEDGMENTS

We acknowledge the Swiss National Center of Competence in Research on Nanoscale Science, the National Science Foundation, and the European Science Foundation EUROCORES Programme FANAS for financial support.

#### APPENDIX

Two effective springs are used in the simulations, one for the  $x$  direction and the other for the  $y$  direction. Each of these effective springs represents the effect of several springs that are coupled in series. According to Carpick *et al.*<sup>37</sup> the effective spring constant is the reciprocal sum of the single spring constants,

$$k_{\text{eff}} = \left( \frac{1}{k_{\text{lateral}}} + \frac{1}{k_{\text{contact}}} \right)^{-1}, \quad (\text{A1})$$

where  $k_{\text{lateral}}$  is lateral spring constant of the cantilever and  $k_{\text{contact}}$  is the lateral contact stiffness that describes the elastic deformation of the tip apex and the surface in contact at a given load. According to independent measurements on different systems<sup>4,8,12,35</sup> the lateral contact stiffness  $k_{\text{contact}}$  is the softest spring and thus essential and decisive for  $k_{\text{eff}}$ . The lateral spring constant  $k_{\text{lateral}}$  is in general different for the  $x$  and  $y$  directions. The  $x$  direction, which is the scan direction in the experiment, is perpendicular to the cantilever. Again, two springs contribute to the lateral spring of the cantilever: the torsion of the cantilever with its torsional spring constant  $k_{\text{tors}}$  and the *in-plane bending* of the cantilever with the bending spring constant  $k_{\text{bend}}$ . The torsional spring constant of a rectangular cantilever is<sup>38</sup>

$$k_{\text{tors}} = \frac{Gwr^3}{3h^2l}, \quad (\text{A2})$$

where  $G$  is the shear modulus,  $w$  is the width,  $t$  is the thickness,  $l$  is the length of the cantilever, and  $h$  is the tip height. The bending spring constant is<sup>39</sup>

$$k_{\text{bend}} = \frac{Et w^3}{4l^3}, \quad (\text{A3})$$

where  $E$  is the elasticity modulus of the cantilever. The torsional and bending spring constants are then combined to give the lateral spring constant in the  $x$  direction,<sup>39</sup>

$$k_{x\text{-lateral}} = \left( \frac{1}{k_{x\text{-tors}}} + \frac{1}{k_{x\text{-bend}}} \right)^{-1}. \quad (\text{A4})$$

With typical cantilevers used in the experiment (Nanosensors, type: PPP-CONTR), a value of  $k_{x\text{-lateral}} \approx 25$  N/m is estimated. It is well known that the effective spring constant  $k_{x\text{-eff}}$  in the  $x$  direction can be extracted from the slope of the sticking part in the stick-slip curve.<sup>8</sup> Due to the reciprocal addition of the spring constants [see Eq. (A1)], the effective spring constant  $k_{\text{eff}}$  is dominated by the weakest spring. Usually a relatively low effective spring constant is found in the experiment, of the order of  $k_{x\text{-eff}} \approx 2$  N/m,<sup>16</sup> which is considerably lower than the lateral spring constant  $k_{x\text{-lateral}}$  itself.

Hence the effective spring constant  $k_{x\text{-eff}}$  in the  $x$  direction is primarily determined by the lateral contact stiffness, which is  $k_{x\text{-contact}} \approx 2.2$  N/m for the values above. However the lateral contact stiffness depends strongly on the contact size and hence can vary significantly between tips with differing apex radii. In the simulation the spring constant for the  $x$  direction is kept constant at  $k_{x\text{-eff}} = 2$  N/m.

The determination of the spring constant in the  $y$  direction is more difficult than for the  $x$  direction. In principle Eq. (A1) is also valid for the  $y$  direction, but it is difficult to quantitatively analyze stick-slip motion in parallel to the cantilever in the experiment.<sup>40</sup> Therefore an effective spring constant  $k_{y\text{-eff}}$  can only be approximately estimated. The contact stiffness  $k_{\text{contact}}$  is assumed to be equal in both directions, and the lateral spring constant  $k_{y\text{-lateral}}$  of the cantilever is given by<sup>39</sup>

$$k_{y\text{-lateral}} = \frac{Ewt^3}{12h^2l}. \quad (\text{A5})$$

Inserting the experimental values,  $k_{y\text{-lateral}} \approx 25$  N/m is obtained. It is remarkable that the lateral spring constant for both the  $x$  direction and  $y$  direction are in the same range. Because the effective spring constant  $k_{y\text{-eff}}$  is not known from the experiment, this parameter is varied in the simulations (see Sec. III A).

\*pascal.steiner@unibas.ch

<sup>†</sup>Present address: Materials Science Division, Lawrence Berkeley National Laboratory, Cyclotron Road 1, CA 94720, USA.

<sup>1</sup>M. Mate, G. M. McClelland, R. Erlanson, and S. Chiang, *Phys. Rev. Lett.* **59**, 1942 (1987).

<sup>2</sup>L. Howald *et al.*, *Appl. Phys. Lett.* **63**, 117 (1993).

<sup>3</sup>E. Gnecco, R. Bennewitz, T. Gyalog, C. Loppacher, M. Bamberlin, E. Meyer, and H. J. Guntherodt, *Phys. Rev. Lett.* **84**, 1172 (2000).

<sup>4</sup>E. Riedo, E. Gnecco, R. Bennewitz, E. Meyer, and H. Brune, *Phys. Rev. Lett.* **91**, 084502 (2003).

<sup>5</sup>S. Morita, S. Fujisawa, and Y. Sugawara, *Surf. Sci. Rep.* **23**, 1 (1996).

<sup>6</sup>G. A. Tomlinson, *Philos. Mag.* **7**, 905 (1929).

<sup>7</sup>I. Szlufarska, M. Chandross, and R. Carpick, *J. Phys. D* **41**, 123001 (2008).

<sup>8</sup>A. Socoliuc, R. Bennewitz, E. Gnecco, and E. Meyer, *Phys. Rev. Lett.* **92**, 134301 (2004).

<sup>9</sup>M. Dienwiebel, G. S. Verhoeven, N. Pradeep, J. W. M. Frenken, J. A. Heimberg, and H. W. Zandbergen, *Phys. Rev. Lett.* **92**, 126101 (2004).

<sup>10</sup>G. S. Verhoeven, M. Dienwiebel, and J. W. M. Frenken, *Phys. Rev. B* **70**, 165418 (2004).

<sup>11</sup>A. E. Filippov, M. Dienwiebel, J. W. M. Frenken, J. Klafter, and M. Urbakh, *Phys. Rev. Lett.* **100**, 046102 (2008).

<sup>12</sup>A. Socoliuc *et al.*, *Science* **313**, 207 (2006).

<sup>13</sup>E. Gnecco, A. Socoliuc, S. Maier, J. Gessler, T. Glatzel, A. Baratoff, and E. Meyer, *Nanotechnology* **20**, 025501 (2009).

<sup>14</sup>E. Gnecco, A. Socoliuc, and E. Meyer, in *Superlubricity*, edited

by A. Erdemir and J.-M. Martin (Elsevier, Amsterdam, 2007).

<sup>15</sup>H. Hölscher, U. Schwarz, and R. Wiesendanger, *Surf. Sci.* **375**, 395 (1997).

<sup>16</sup>T. Filleter, W. Paul, and R. Bennewitz, *Phys. Rev. B* **77**, 035430 (2008).

<sup>17</sup>H. Hölscher, U. D. Schwarz, O. Zwörner, and R. Wiesendanger, *Z. Phys. B: Condens. Matter* **104**, 295 (1997).

<sup>18</sup>I. Horcas *et al.*, *Rev. Sci. Instrum.* **78**, 013705 (2007).

<sup>19</sup>P. Langevin, *C. R. Hebd. Seances Acad. Sci.* **146**, 530 (1908).

<sup>20</sup>Y. Sang, M. Dubé, and M. Grant, *Phys. Rev. Lett.* **87**, 174301 (2001).

<sup>21</sup>P. Reimann and M. Evstigneev, *New J. Phys.* **7**, 25 (2005).

<sup>22</sup>M. P. Allen and D. J. Tildesley, *Computer Simulation of Liquids* (Clarendon, Oxford, 1990).

<sup>23</sup>T. Gyalog and H. Thomas, *Europhys. Lett.* **37**, 195 (1997).

<sup>24</sup>E. Gnecco, R. Bennewitz, T. Gyalog, and E. Meyer, *J. Phys.: Condens. Matter* **13**, R619 (2001).

<sup>25</sup>T. Gyalog *et al.*, *Europhys. Lett.* **31**, 269 (1995).

<sup>26</sup>C. Fusco and A. Fasolino, *Appl. Phys. Lett.* **84**, 699 (2004).

<sup>27</sup>U. Wyder, A. Baratoff, and E. Meyer, *J. Vac. Sci. Technol. B* **25**, 1547 (2007).

<sup>28</sup>R. Lüthi *et al.*, *J. Vac. Sci. Technol. B* **14**, 1280 (1996).

<sup>29</sup>N. Sasaki, K. Kobayashi, and M. Tsukada, *Phys. Rev. B* **54**, 2138 (1996).

<sup>30</sup>M. Dienwiebel *et al.*, *Surf. Sci.* **576**, 197 (2005).

<sup>31</sup>Y. Sang, M. Dubé, and M. Grant, *Phys. Rev. E* **77**, 036123 (2008).

<sup>32</sup>S. Y. Krylov, K. B. Jinesh, H. Valk, M. Dienwiebel, and J. W. M. Frenken, *Phys. Rev. E* **71**, 065101(R) (2005).

- <sup>33</sup>P. Reimann and M. Evstigneev, *New J. Phys.* **7**, 25 (2005).
- <sup>34</sup>T. Zykova-Timan, D. Ceresoli, and E. Tosatti, *Nature Mater.* **6**, 230 (2007).
- <sup>35</sup>S. Y. Krylov, J. A. Dijksman, W. A. van Loo, and J. W. M. Frenken, *Phys. Rev. Lett.* **97**, 166103 (2006).
- <sup>36</sup>S. Krylov and J. Frenken, *J. Phys.: Condens. Matter* **20**, 354003 (2008).
- <sup>37</sup>R. W. Carpick, D. F. Ogletree, and M. Salmeron, *Appl. Phys. Lett.* **70**, 1548 (1997).
- <sup>38</sup>E. Meyer, R. M. Overney, K. Dransfeld, and T. Gyalog, *Friction and Rheology on the Nanometer Scale* (World Scientific, Singapore, 1998).
- <sup>39</sup>J. Colchero, E. Meyer, and O. Marti, in *Handbook of Micro/Nano Tribology*, edited by B. Bhushan (CRC, Ohio, 1999).
- <sup>40</sup>S. Fujisawa, K. Yokoyama, Y. Sugawara, and S. Morita, *Phys. Rev. B* **58**, 4909 (1998).